



Combined Kalman and sliding innovation filtering: An adaptive estimation strategy

Andrew S. Lee^a, Waleed Hilal^b, S. Andrew Gadsden^{b,*}, M. Al-Shabi^c

^a College of Engineering and Physical Sciences at the University of Guelph, Ontario, Canada

^b Department of Mechanical Engineering at McMaster University, Ontario, Canada

^c Department of Mechanical and Nuclear Engineering, University of Sharjah, Sharjah, United Arab Emirates

ARTICLE INFO

Keywords:

Estimation theory
Kalman filter
Magnetorheological damper
Modeling uncertainty observers
Robustness
Sliding mode
Sliding innovation filter
State-space
Unscented
Variable boundary layer

ABSTRACT

This paper proposes a new adaptive estimation strategy for a nonlinear system with modeling uncertainties. The extended Kalman filter (EKF) and unscented Kalman filter (UKF) are optimal estimators which have been used extensively for state estimation in literature and industry. While the EKF uses a first order Taylor series expansion to approximate nonlinearities, the UKF uses sigma points from the projected probability distribution of states. The sliding innovation filter (SIF) is a suboptimal, yet robust estimation strategy which has recently been proposed. For nonlinear systems, the extended SIF (ESIF) is formulated by using a first order Taylor series expansion like the EKF. This work proposes a novel adaptive estimation strategy which combines and balances the optimality of the EKF and UKF with the robustness of the ESIF. These new methods are referred to as the EKF-ESIF and UKF-ESIF, respectively. A time-varying sliding boundary layer is used as a means of detecting the presence of faults or uncertainties and as a criterion for switching between the EKF or UKF and the ESIF. In normal operating conditions the algorithm computes estimates using an optimal KF-based gain, and an SIF-based gain when a fault is detected. The system examined in this study consists of a magnetorheological (MR) damper with a constant current. Faults or uncertainties are introduced as unwanted behavior in the power supply in the form of undercurrent and overcurrent. The robustness of the EKF-ESIF and UKF-ESIF was validated for force estimation exerted by the MR damper and the results were compared with the standard EKF and UKF.

1. Introduction

THE goal of estimation theory is to extract information from systems with uncertainty. This uncertainty may stem from noise, disturbances, or inaccuracies in the system model. In control systems, accurate estimates are vital for feedback loops. The Kalman filter (KF) produces the optimal estimate for systems with white noise (or normal distribution with zero mean) [1]. Optimality is achieved through minimizing the trace of the state error covariance matrix which is a measure of state estimation error [1–4]. Due to its optimality and simple corrective gain calculation, the KF is very popular estimator with numerous applications such as fault detection, tracking, and system parameter estimation [5]. However, most systems in nature exhibit nonlinear behavior or have non-Gaussian noise distributions. In addition, it is possible that an estimator does not have full knowledge of the system resulting in modeling uncertainty [1]. Thus, current research in estimation theory

seeks to improve estimation accuracy in these scenarios.

As with control theory, there exists a trade-off between estimation accuracy and robustness. While the KF is optimal under certain conditions, disturbances can cause the estimates to become unstable. Modern estimation theory aims to increase estimation accuracy while simultaneously achieving robustness to noise, disturbances, and modeling uncertainty.

Several strategies for approximating nonlinearities in systems models have been proposed in literature. One of the most popular methods, the extended Kalman filter (EKF), linearizes the system around the *a priori* (predicted) state estimate [1,6,7]. Specifically, a first-order Taylor series approximation of the system model is calculated to produce a Jacobian matrix. This matrix is used to generate the *a priori* state error covariance matrix. For highly-nonlinear systems, the Jacobian matrix is not an appropriate approximation and may cause the EKF estimates to diverge from the true state trajectory which can lead to poor

* Corresponding author.

E-mail addresses: alee32@uoguelph.ca (A.S. Lee), hilalw@mcmaster.ca (W. Hilal), gadsden@mcmaster.ca (S. Andrew Gadsden), malshabi@sharjah.ac.ae (M. Al-Shabi).

<https://doi.org/10.1016/j.measurement.2023.113228>

Received 29 October 2022; Received in revised form 1 June 2023; Accepted 16 June 2023

Available online 25 June 2023

0263-2241/© 2023 Elsevier Ltd. All rights reserved.

estimates and numerical instability [8].

Another way to capture nonlinear behavior of a system is through sample points. The sigma point Kalman filter (SPKF) uses weighted statistical linear regression to approximate the nonlinearities [9]. The sigma points are generated from a projected probability distribution of the states that are propagated through the nonlinear system model [9]. This method does not require local linearization and generally produces more accurate estimates when compared to the EKF [10].

The unscented Kalman filter (UKF) is a popular variant of the SPKF. A deterministic sampling approach known as the unscented transform is used to select a minimal number of sampling points around the previous state estimate [9]. Monte Carlo sampling can be used to approximate the mean and covariance of the updated states. The UKF can approximate the statistical mean and covariance for any nonlinearity up to the third order [8]. This generally makes the UKF superior to the EKF which uses a first-order approximation, especially for increasingly nonlinear systems. The tradeoff for increased accuracy in this case is increased computational cost which may result in lower sample rates for real-time systems.

Sliding mode observer (SMOs) are based on variable structure control and systems introduced in the 1950s [8]. The observer gains are produced as a function of the innovation (measurement error). The error surface moves towards the origin in an ideal scenario [11]. SMOs define a sliding surface (or hyperplane) to apply a discontinuous switching force that keeps the estimates within an area of the sliding surface [11]. The smooth variable structure filter (SVSF) is a model-based estimator formulated on SMO concepts [12].

The corrective gain for the SVSF is calculated using the measurement error and a switching term. The corrective gain forces the estimates to remain in an area of the hyperplane [12]. While the switching structure of the gain adds stability and robustness, the state estimates can be prone to chatter when the smoothing boundary layer is too narrow. Since its original formulation in 2007, the SVSF has been expanded to incorporate an adaptive smoothing boundary layer [12]. Further improvements have been made on SVSF that include the use of a chattering function for multi-target tracking, higher order solutions, and fault detection [13]. More importantly, an adaptive formulation of the SVSF has been proposed, where it has been implemented alongside the KF in [14]. The findings in [14], show that such an approach demonstrates improved estimation performance, and thus serving as one of the main inspirations behind this research.

The sliding innovation filter (SIF) was first presented in 2020 and is based on SMOs like the SVSF [15]. The SIF improves upon the SVSF formulation through a simpler, more concise gain calculation and produces more accurate state estimates [15]. The originally formulation of the SIF uses a fixed sliding boundary layer and was expanded to incorporate the state error covariance in the corrective gain calculation. An adaptive formulation of the SIF, termed the ASIF, was presented in [16] and minimizes the state error covariance which results in a time-varying sliding boundary layer. This time-varying sliding boundary layer is a function of the innovation, its covariance, and the state error covariance and can be used as a metric for measuring modeling uncertainty. Several other works propose modified formulations of the SIF geared towards improving the filter's performance for target tracking applications [17,18].

Many adaptive estimation strategies have also been proposed in the literature, an area which has been experiencing rapid growth in recent years. Adaptive estimation methods enable traditional filters such as the KF to dynamically update certain parameters of the algorithm, such as the system and measurement models, or their respective noise covariances as in [19] and [20]. Several adaptive methods have also been proposed to address the degradation of performance associated with the KF in the face of non-Gaussian noise [21–23], and in the presence of measurement outliers [23,24]. For more examples of adaptive estimation techniques and applications, we refer the reader to [25–29].

Other types of adaptive estimation methods, such as the one in [14] and as will be proposed by this paper, utilize a mechanism to detect the

presence of undesired factors such as faults, disturbances, or modelling uncertainties, and can subsequently switch between several different filters.

In this paper, the time-varying sliding boundary layer is used to propose two new adaptive estimation strategies that combine the EKF and UKF with an extended version of the SIF for nonlinear systems called the ESIF. This paper presents a method for switching between the EKF/UKF and ESIF when a system model is well-defined or contains modeling uncertainties, respectively, using the time-varying sliding boundary layer. Experimental simulations are carried out on a magnetorheological (MR) damper test bed with constant current input. Faults are simulated in the system by means of overcurrent and undercurrent from the power supply. The goal of the approach proposed in this study is to output an optimal KF-based estimate in normal operating conditions, and a robust SIF-based estimate in the presence of a fault by using the time-varying boundary layer as a means of detecting the fault.

The paper is organized as follows. An overview of the estimation methods used in this paper are provided in Section 2. The proposed adaptive approach is described in Section 3, followed by an exposition on the experimental setup in Section 4. A discussion of the results may be found in Section 5, followed by concluding remarks and future work in Section 6.

2. Estimation methods

2.1. Extended Kalman filter

The EKF is an extension of the KF for nonlinear dynamic systems. The system is linearized around the predicted (or *a priori*) state estimate $\hat{x}_{k+1|k}$, where k is the time step, in order to calculate the *a priori* state error covariance, innovation, and corrective Kalman gain [1]. A first order Taylor series expansion of the nonlinear system model f and measurement process h are used to generate respective Jacobian matrices, F_{k+1} and H_{k+1} , respectively. This is done because the nonlinear equations cannot be applied directly to the state error covariance terms [10]. Otherwise, the rest of the EKF's procedure is identical to that of the KF, and can be summarized as follows.

The prediction stage is completed by calculating the *a priori* state error covariance matrix $P_{k+1|k}$, as follows [10]:

$$P_{k+1|k} = F_{k+1}P_{k|k}F_{k+1}^T + Q_k \quad (2.1.1)$$

where $P_{k|k}$ is the previous state error covariance, Q_k is the system noise covariance matrix and T is the matrix transpose operator.

In the update stage, the Kalman gain, K_{k+1} is used to calculate the *a posteriori* estimate, $\hat{x}_{k+1|k+1}$, and *a posteriori* state error covariance $P_{k+1|k+1}$ using the following equations [10]:

$$K_{k+1} = P_{k+1|k}H_{k+1}^T [H_{k+1}P_{k+1|k}H_{k+1}^T + R_{k+1}]^{-1} \quad (2.1.2)$$

$$\hat{x}_{k+1|k+1} = \hat{x}_{k+1|k} + K_{k+1} [z_{k+1} - H_{k+1}\hat{x}_{k+1|k}] \quad (2.1.3)$$

$$P_{k+1|k+1} = [I - K_{k+1}H_{k+1}]P_{k+1|k}[I - K_{k+1}H_{k+1}]^T + K_{k+1}R_{k+1}K_{k+1}^T \quad (2.1.4)$$

where z_{k+1} is the measurement, R_{k+1} is the measurement noise covariance matrix and I is the identity matrix. Implementing the EKF can be problematic if the Jacobian matrix cannot be derived easily. In addition, the EKF can only handle a limited level of nonlinearities. The UKF is generally better suited for higher order nonlinear systems.

2.2. Unscented Kalman filter

The UKF uses the unscented transform to approximate nonlinear processes. This deterministic sampling approach selects a minimal number of sample points, known as sigma points, around the previous

state estimate [1]. The sigma points are propagated through the nonlinear system model and measurement process and used to approximate the system mean and covariance. While the UKF is better able to account for nonlinearities and arbitrary distributions, it is more computationally expensive than the EKF. The UKF algorithm is summarized as follows.

The state vector can be approximated by $2n + 1$ sigma points, where n is the dimension of the state vector. The i^{th} sigma point $\chi_{k|k}^i$ is calculated as follows [1]:

$$\begin{cases} \chi_{k|k}^0 = \hat{x}_{k|k}, & i = 0 \\ \chi_{k|k}^i = \hat{x}_{k|k} + \sqrt{(n + \kappa)(P_{k|k})_i}, & i = 1, \dots, n \\ \chi_{k|k}^{i+n} = \hat{x}_{k|k} - \sqrt{(n + \kappa)(P_{k|k})_i}, & i = 1, \dots, n \end{cases} \quad (2.2.1)$$

where κ is a scaling factor and design parameter. The associated weight w_i of the samples determined as follows [1]:

$$w_i = \begin{cases} \frac{\kappa}{n + \kappa}, & i = 0 \\ \frac{1}{2(n + \kappa)}, & i = 1, \dots, 2n \end{cases} \quad (2.2.2)$$

The *a priori* state estimate $\hat{x}_{k+1|k}$ and *a priori* state error covariance $P_{k+1|k}$ are calculated by propagating the sigma points as follows [1]:

$$\chi_{k+1|k}^i = f(\chi_{k|k}^i) \quad (2.2.3)$$

$$\hat{x}_{k+1|k} = \sum_{i=0}^{2n} w_i \chi_{k+1|k}^i \quad (2.2.4)$$

$$P_{k+1|k} = \sum_{i=0}^{2n} w_i [\chi_{k+1|k}^i - \hat{x}_{k+1|k}] [\chi_{k+1|k}^i - \hat{x}_{k+1|k}]^T + Q_k \quad (2.2.5)$$

The prediction stage measurements are also propagated as follows [1]:

$$\xi_{k+1|k}^i = h(\chi_{k+1|k}^i) \quad (2.2.6)$$

$$\hat{z}_{k+1|k} = \sum_{i=0}^{2n} w_i \xi_{k+1|k}^i \quad (2.2.7)$$

In the update stage, the *a posteriori* state error covariance $P_{z,k+1|k}$ and innovation covariance $P_{yz,k+1|k}$ are used to calculate the UKF corrective gain K_{k+1} as follows [1]:

$$P_{z,k+1|k} = \sum_{i=0}^{2n} w_i [\xi_{k+1|k}^i - \hat{z}_{k+1|k}] [\xi_{k+1|k}^i - \hat{z}_{k+1|k}]^T + R_{k+1} \quad (2.2.8)$$

$$P_{yz,k+1|k} = \sum_{i=0}^{2n} w_i [\chi_{k+1|k}^i - \hat{x}_{k+1|k}] [\xi_{k+1|k}^i - \hat{z}_{k+1|k}]^T \quad (2.2.9)$$

$$K_{k+1} = P_{yz,k+1|k} P_{z,k+1|k}^{-1} \quad (2.2.10)$$

Finally, the *a posteriori* state estimate $\hat{x}_{k+1|k+1}$ and *a posteriori* state error covariance $P_{k+1|k+1}$ are updated as follows [1]:

$$\hat{x}_{k+1|k+1} = \hat{x}_{k+1|k} + K_{k+1} (z_{k+1} - \hat{z}_{k+1|k}) \quad (2.2.11)$$

$$P_{k+1|k+1} = P_{k+1|k} - K_{k+1} P_{z,k+1|k} K_{k+1}^T \quad (2.2.12)$$

2.3. Extended sliding innovation filter

The sliding innovation filter (SIF) is a Bayesian, model-based estimator formulated on SMO concepts. While similar to the KF, the SIF features a different corrective gain that incorporates a sliding boundary

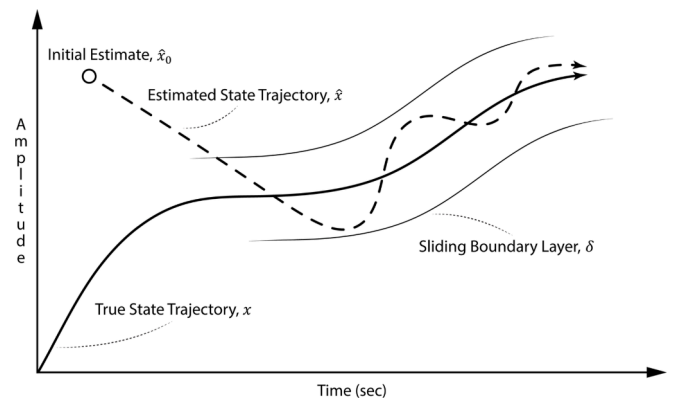


Fig. 1. The sliding innovation filter (SIF) concept depicting the effect of the sliding boundary layer and SIF switching gain [15].

layer [15]. The SIF gain is a function of the measurement matrix (or measurement Jacobian), the innovation (measurement error), and sliding boundary layer widths. The sliding boundary layer widths are a user defined parameter based on the upper limit of uncertainties in the estimation process due to modeling uncertainty and noise. The widths and are generally chosen based on practitioner's knowledge or experience, or tuned manually otherwise [15]. Previous state estimates are forced towards the sliding boundary layer by the corrective gain. However, if the estimates are already within the boundary layers limits, the estimates switch about the true state trajectory [15]. The SIF estimation concept is depicted in Fig. 1.

For system models and measurement processes that are nonlinear, the extended sliding innovation filter (ESIF) may be used. The ESIF has an identical prediction stage to the EKF. Nonlinear behavior is also approximated by first order Taylor series. The prediction stage of the ESIF is given as follows [15]:

$$\hat{x}_{k+1|k} = f(\hat{x}_{k|k}, u_k) \quad (2.3.1)$$

$$P_{k+1|k} = F_{k+1} P_{k|k} F_{k+1}^T + Q_k \quad (2.3.2)$$

While the system used in this paper is nonlinear, the measurement process is linear and constant. For simplicity, the measurement matrix is denoted by C . The update stage is given by the following [15]:

$$|\tilde{z}_{k+1|k}| = |z_{k+1} - C\hat{x}_{k+1|k}| \quad (2.3.3)$$

$$K_{k+1} = C^+ \overline{\text{sat}} \left(\frac{|\tilde{z}_{k+1|k}|}{\delta} \right) \quad (2.3.4)$$

$$\hat{x}_{k+1|k+1} = \hat{x}_{k+1|k} + K_{k+1} \tilde{z}_{k+1|k} \quad (2.3.5)$$

$$P_{k+1|k+1} = (I - K_{k+1} C) P_{k+1|k} (I - K_{k+1} C)^T + K_{k+1} R_{k+1} K_{k+1}^T \quad (2.3.6)$$

where $|\tilde{z}_{k+1|k}|$ refers to the absolute value of the innovation, C^+ is the pseudoinverse of the measurement Jacobian, $\overline{\text{sat}}$ refers to the diagonal matrix of the saturated vector values, and δ refers to the sliding boundary layer width [15]. The SIF gain K_{k+1} is applied to the innovation $\tilde{z}_{k+1|k}$ and the *a priori* state estimate $\hat{x}_{k+1|k}$ in the same fashion as the KF. The calculation of the *a posteriori* state error covariance $P_{k+1|k+1}$ is also identical to the KF [15].

It can be helpful to illustrate the SIF gain by considering a simple example of a system with two measurements (and $C = I$) such that the saturation term in (2.3.4) can be expanded further:

$$K_{k+1} = C^+ \overline{\text{sat}} \left(\left| \tilde{z}_{k+1|k} \right| / \delta \right)$$

$$= \begin{bmatrix} \text{sat} \left(\frac{|\tilde{z}_1|}{\delta_1} \right) & 0 \\ 0 & \text{sat} \left(\frac{|\tilde{z}_2|}{\delta_2} \right) \end{bmatrix} \quad (2.3.7)$$

When multiplied with the innovation $\tilde{z}_{k+1|k}$ as in (2.3.5), the state estimates $\hat{x}_{k+1|k}$ are updated with the following term:

$$K_{k+1} \tilde{z}_{k+1|k} = \begin{bmatrix} \text{sat} \left(\frac{|\tilde{z}_1|}{\delta_1} \right) \tilde{z}_1 \\ \text{sat} \left(\frac{|\tilde{z}_2|}{\delta_2} \right) \tilde{z}_2 \end{bmatrix} \quad (2.3.8)$$

As shown in the (2.3.8), the state estimates are updated with their corresponding innovation and sliding boundary layer term. The SIF gain effectively acts as a switching term which forces the measurement errors to be bounded towards the true state trajectory. The term within the saturation function is responsible for judging whether the state lies within, or outside the border. The state estimates are within the sliding boundary layer when the proportion of the absolute value of the innovation is less than one, and thus the value of this proportion is unaffected by the saturation term. If the state estimates are beyond the sliding boundary layer, the value of this proportion would be greater or equal to one, and is consequently saturated to a value of one by the saturation term.

3. Proposed combined Kalman and sliding innovation filtering strategies

A time-varying sliding boundary layer δ_{vbl} was derived in [16], and is computed at each timestep to replace the fixed sliding boundary layer δ . This time-varying boundary layer forms the basis of the adaptive SIF strategy and is given by the following equations as defined in [16]:

$$S_{k+1} = CP_{k+1|k}C^T + R_{k+1} \quad (3.1)$$

$$\delta_{vbl} = S_{k+1} (CP_{k+1|k}C^T)^{-1} \left| \overline{\tilde{z}_{k+1|k}} \right| \quad (3.2)$$

where S_{k+1} is the innovation matrix and $\left| \overline{\tilde{z}_{k+1|k}} \right|$ is the absolute magnitude of the innovation. The innovation matrix is a term which was also newly derived in [16], and as shown in (3.1), is a function of the *a priori* state error covariance, measurement matrix, and measurement noise covariance. No other use exists for the innovation matrix other than to compute the time-varying sliding boundary layer at each timestep. On a side note, it is theoretically possible to improve the SIF results for a well-defined system by computing an average of the time-varying boundary layer and setting the fixed boundary layer width δ to that value. This results in a well-tuned existence subspace [16]. However, this approach is rather counterproductive as it would be more conducive to go forth with implementing the ASIF due to its improved performance.

The proposed estimation strategy uses the EKF and UKF estimators when the time-varying boundary layer is below a certain threshold, δ_{lim} . When the time-varying boundary layer exceeds the threshold, the ESIF gain is used instead to compensate for the increased modeling uncer-

tainty. In this paper, the experimentally determined δ_{lim} represents a significant change in the system model due to faults in the power supply, which results in a deviation in the MR damper behavior. However, if the measurement noise is too high, the threshold may not represent a clear boundary between the normal and faulty modes.

For implementation, the *a priori* state estimate and *a priori* state error covariance matrix are calculated first. The time varying boundary layer, δ_{vbl} , is then calculated and compared with the experimentally determined threshold value, δ_{lim} . If the time varying boundary layer is smaller than the threshold, the EKF or UKF gain is used to update the state estimates and state error covariance. However, if the boundary layer value is larger than the threshold, the ESIF gain is implemented using the fixed boundary layer width, δ . Thus, the δ_{vbl} is not used in the computation of any of the filter's gains and is merely an indicator of the presence of an uncertainty or fault and when to switch between the EKF/UKF and the ESIF gains.

4. Experimental setup

4.1. Description

The primary component in the experimental setup used in this paper is the RD-8041-1 MR damper acquired from LORD [30]. MR dampers have numerous applications in the automotive and aerospace industry such as isolating vibrations to passengers using adaptive suspension systems [31]. A typical MR damper consists of the MR fluid itself, housing, piston, diaphragm, and magnetic coil. An electrical current is supplied to the damper to increase the viscosity of the MR fluid which in turn, increases the damping force. The change in viscosity is attributed to the rearrangement of the ferromagnetic particles suspended in the fluid. In the presence of a magnetic field, the particles align to form linear chain structures. As the MR damper is driven, the MR fluid moves between different chambers via small orifices in the piston assembly and converts mechanical energy into friction losses.

The experimental setup was developed at the University of Guelph by the primary author. In order to mathematically model the MR damper, an A1 series linear actuator from UltraMotion was used to drive the damper [32]. A RAS1-500S-S resistive load cell acquired from Loadstar [33] was used to measure the damping force and a programmable power supply was used to supply current to the MR damper. Data acquisition and commands were delivered using RS232 serial communication on a laboratory computer. The components were mounted together using an extruded t-slotted aluminum frame as seen in Fig. 2.

The RD-8041-1 is a linear MR damper with continuous variable damping force determined by the yield strength of the MR fluid (which in turn is determined by the magnetic field). The MR fluid responds in less than 15 ms to changes in the magnetic field and can operate at 1 A continuously or 2 A intermittently at 12 V DC. The RD-8041-1 is a monotube shock containing high pressure nitrogen gas (300 psi) which fully extends the piston under no load. At ambient temperatures the resistance of the coil is 5 Ω and at 71° C the resistance increases to 7 Ω . Extreme temperature changes can drastically alter the performance of

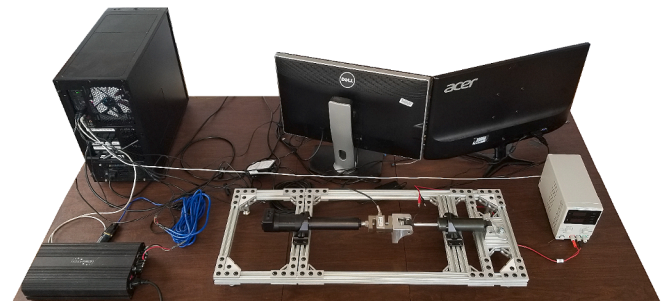


Fig. 2. Magnetorheological test bed used in this study.

the MR damper [34].

The Ultramotion linear actuator used to drive the MR damper is a standard servo cylinder with an acme screw to prevent backdrive and operates at 180 W. The actuator is capable of 445 N of continuous force and 1001 N at its peak with a maximum speed of 178 mm/s. There are several onboard sensors to measure states such as position, torque, temperature, and humidity. The position of the linear actuator is measured using the phase index absolute position sensor. This sensor is a multi-turn battery-less magnetic encoder with a resolution of 1024 counts per revolution used for absolute position feedback and commutation. The measurement noise covariance of the sensor is discussed in subsequent sections. The torque feedback is calculated using closed loop current feedback on each motor phase. This is then translated into actuator output force. Since using current feedback is not an accurate method of calculating output force resulting in high error and noise.

In general, there is a direct relationship between motor torque and actuator output force. However, there are some complicating factors that can significantly impact this relationship. Rotational inertial loads, lubricant viscosity, and seal friction can all contribute to output force variability. Factory test data was used in order to convert motor torque into actuator output force. The data is collected on each actuator during the acceptance test procedure (ATP) before leaving the factory. The current-force curves that are generated are unique to each actuator. However, there is still significant noise in force output. In order to reduce some of the noise in the torque sensor, a first order Butterworth filter was applied with a cutoff frequency between 0 and 0.3 of the Nyquist rate.

The RAS1-500S-S is a resistive S-Beam load cell capable of measuring both compressive and tensile force measurement. The load cell is made from tool steel and has a capacity of 2224 N and a sample rate of 1000 Hz. The calibration measurement equipment is traceable to NIST via Pacific Calibration Services. This sensor was used to test the efficacy of applying adaptive filtering strategies on the motor torque sensor of the linear actuator. While the noise covariance of the loadcell is 26.535 N, the noise covariance of the Ultramotion motor torque sensor is 622.407 N. The comparatively high noise distribution of the onboard Ultramotion motor torque sensor makes it a suitable candidate for applying adaptive filtering strategies.

Force-velocity hysteresis curves have been modeled extensively by [35] and [36]. However, at low velocities over long stroke lengths, the force of the diaphragm and compressed nitrogen gas is not negligible. Thus, a force-position curve was modeled by driving the MR damper at a constant velocity over one full stroke. For the MR model used in this paper, the actuator speed was set to 41.5 mm/s and the damping force was recorded by the loadcell over a stroke length of 57 mm. Approximately 200 S (extension and retraction) were used to model the behavior of the behavior at each operational mode (normal, overcurrent, undercurrent). The conditions of the operational modes are discussed below.

We now discuss the conditions of the operational modes encountered by the MR damper, of which there are several different types of faults that can be experienced during MR damper operations. The viscosity of the MR fluid is sensitive to extreme temperatures and the particles in the MR fluid are also subject to degradation over time [37]. However, this paper focuses on faults introduced in the current supplied to MR damper through minor temperature changes or faulty power supplies. Undercurrent and overcurrent fault modes were modeled in addition to the normal operating current. The undercurrent, normal, and overcurrent operational modes are denoted by a supply current of 20 mA, 60 mA and 100 mA respectively.

A sample of experimental data used to model the MR damper is shown in Fig. 3. The figures show the actuator extending and retracting at a constant speed with the MR force being recorded by the loadcell and actuator motor torque sensor. The figures also show the application of a first order Butterworth filter on the actuator current sensor in order to reduce some of the noise before applying adaptive filtering strategies.

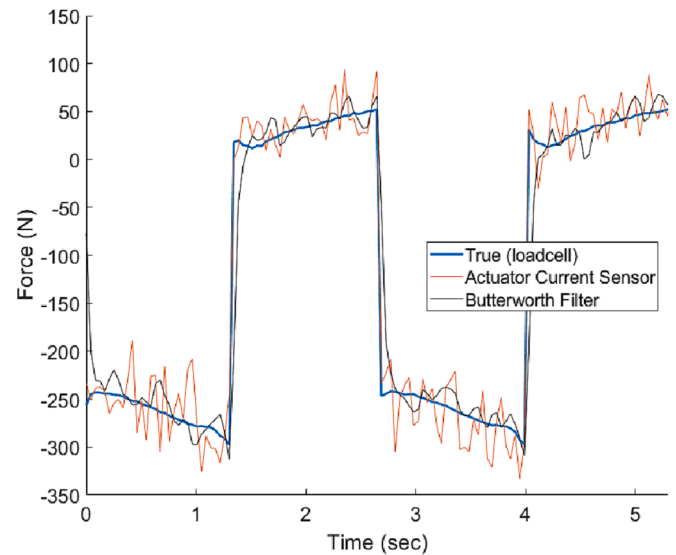


Fig. 3. Sample of experimental data used to model the MR damper under normal operating conditions.

4.2. Magnetorheological damper model

The force-velocity hysteresis of an MR damper has been described in literature using many different mathematical models such as the nonlinear hysteretic biviscous model, polynomial function model, generalized sigmoid hysteresis model, and Bouc-Wen hysteresis model [35]. However, at low velocities and long stroke lengths, the force applied by the diaphragm and compressed nitrogen gas is not negligible. Thus, the relationship between MR damper force and actuator position was further incorporated into the model.

The full mathematical model of the MR damper calculates force as a function of velocity, position, and current applied to the damper. Assuming the current is kept constant, the force becomes a function of position and velocity and can be modeled as a polynomial surface as seen in Fig. 4 and Fig. 5. Since the experiments were conducted using a constant velocity model, the overall system model was further reduced to, as per equation (4.2.2). The overall effect on the full MR model and its force profile is clear from Fig. 6, where it is evident that the position of the actuator is now the only factor affecting the system's force output.

A sixth order polynomial model was chosen for this experiment because it was the least computationally expensive for implementing

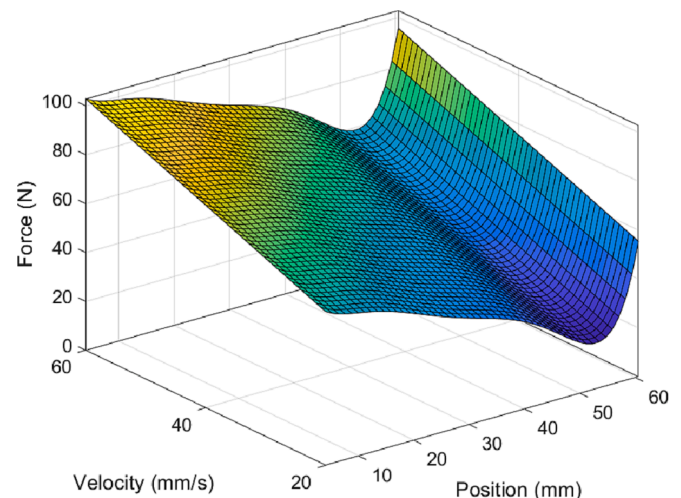


Fig. 4. MR force during extension with respect to position and velocity.

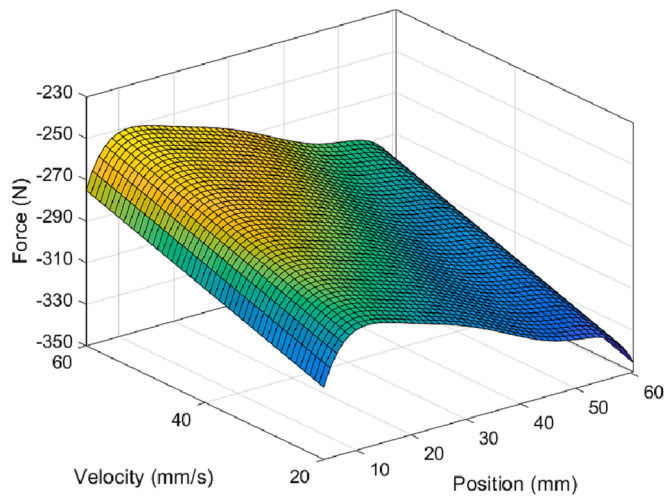


Fig. 5. MR force during retraction with respect to position and velocity.

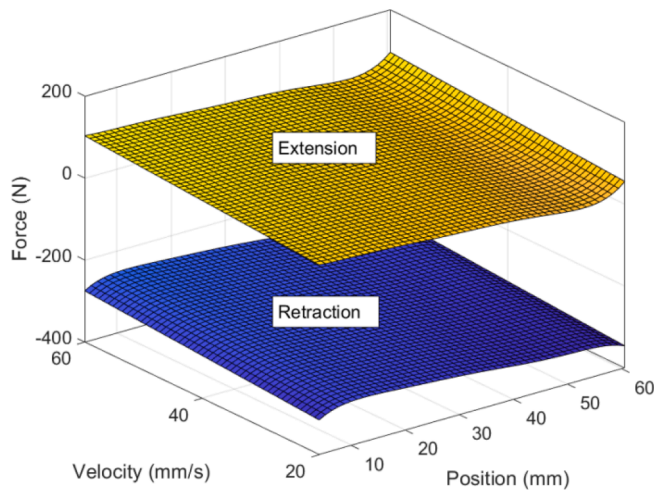


Fig. 6. Full MR force model with extension and retraction with constant velocity.

model-based filters such as the EKF, UKF, and ESIF without sacrificing significant model accuracy. The basic polynomial hysteresis function is as follows [35]:

$$f_i = \sum_{k=0}^n a_k y^k; \quad n = 6 \quad (4.2.1)$$

where y is the position of the MR piston, a_k is the polynomial coefficient constant which is experimentally obtained, k represents the polynomial exponent, and n represents the polynomial order [35]. The velocity (direction) of the piston determines whether the damping force follows the upper or lower hysteresis curve as shown as follows [35]:

$$f_d = \begin{cases} \sum_{k=0}^6 a_{uk} y^k; & \dot{y} < 0 \\ \sum_{k=0}^6 a_{dk} y^k; & \dot{y} > 0 \\ \sum_{k=0}^6 \frac{1}{2} (a_{uk} + a_{dk}) y^k; & \dot{y} = 0 \end{cases} \quad (4.2.2)$$

where a_{uk} and a_{dk} are the lower and upper polynomial coefficients respectively. Convergence of the two polynomial functions near the extremities is ensured through averaging the lower and upper poly-

nomial functions when the piston velocity changes direction or is equal to 0 mm/s [35]. The coefficients of the polynomial model for the normal, undercurrent and overcurrent operating modes are given in Table 1.

The models shown in Fig. 7 depicts the force-position relationship of the MR damper at a velocity of 41.5 mm/s. This represents a cross section of Fig. 6 at the specified velocity. The data points were fitted using (4.2.2) to obtain the polynomial coefficients in Table 1. The norm of the residuals for each data set to their polynomial models are [12.086, 8.1279], [6.794, 8.070], and [7.367, 13.693] for the under current, normal, and over current modes respectively. The first number represents the upper polynomial curve residual while the second represents the lower polynomial curve residual. The discretized state space equations can be written as follows:

$$x_{1,k+1} = x_{1,k} + T \bullet x_{2,k} \quad (4.2.3)$$

$$x_{2,k+1} = x_{2,k} \quad (4.2.4)$$

$$x_{3,k+1} = \begin{cases} \sum_{k=0}^6 a_{uk} x_{1,k}; x_{2,k} < 0 \\ \sum_{k=0}^6 a_{dk} x_{1,k}; x_{2,k} > 0 \\ \sum_{k=0}^6 \frac{1}{2} (a_{uk} + a_{dk}) x_{1,k}; x_{2,k} = 0 \end{cases} \quad (4.2.5)$$

where x_1, x_2, x_3 , are the position, velocity, and force of MR damper and T is the sampling rate. The system and measurement noise covariance matrices are given by the following:

$$Q = R \bullet 10^{-1} \quad (4.2.6)$$

$$R = \begin{bmatrix} 5.5134 \bullet 10^{-4} & 0 & 0 \\ 0 & 7.797 \bullet 10^{-4} & 0 \\ 0 & 0 & 622.407 \end{bmatrix} \quad (4.2.7)$$

The system noise was not measured directly but was assumed to be one magnitude smaller than the measurement noise.

5. Experimental results and discussion

The linear actuator drove the MR damper for a total of 8 s with a constant velocity during extension and retraction (or triangle wave). The position and velocity profile captured by the actuator encoder can be seen in Fig. 8. The initial current of 60 mA was applied to MR damper which represents normal operation. The MR damper was allowed to fully extend and retract before an overcurrent fault (100 mA) was introduced at 2.66 s. The overcurrent fault is introduced in the experiments by adjusting the state space equations' polynomial coefficients accordingly as per Table 1. After another full period of motion, a

Table 1
Experimental coefficients for polynomial MR model.

Polynomial Coefficient	Undercurrent (20 mA)	Normal (60 mA)	Overcurrent (100 mA)
a_{u0}	$-2.467 \cdot 10^2$	$-2.851 \cdot 10^2$	$-3.488 \cdot 10^2$
a_{u1}	6.476	1.673	19.770
a_{u2}	-0.692	-1.213	-1.909
a_{u3}	$3.581 \cdot 10^{-2}$	$6.132 \cdot 10^{-2}$	$9.053 \cdot 10^{-2}$
a_{u4}	$-1.022 \cdot 10^{-3}$	$-1.675 \cdot 10^{-3}$	$-2.305 \cdot 10^{-3}$
a_{u5}	$1.440 \cdot 10^{-5}$	$2.306 \cdot 10^{-5}$	$2.972 \cdot 10^{-5}$
a_{u6}	$-7.943 \cdot 10^{-8}$	$-1.248 \cdot 10^{-7}$	$-1.518 \cdot 10^{-7}$
a_{d0}	53.347	52.975	94.000
a_{d1}	-7.858	-1.067	-4.528
a_{d2}	0.909	0.184	0.578
a_{d3}	$-5.358 \cdot 10^{-2}$	$-1.660 \cdot 10^{-2}$	$-3.88 \cdot 10^{-2}$
a_{d4}	$1.604 \cdot 10^{-3}$	$6.375 \cdot 10^{-4}$	$1.278 \cdot 10^{-3}$
a_{d5}	$-2.364 \cdot 10^{-5}$	$-1.118 \cdot 10^{-5}$	$-2.028 \cdot 10^{-5}$
a_{d6}	$1.352 \cdot 10^{-7}$	$7.303 \cdot 10^{-8}$	$1.232 \cdot 10^{-7}$

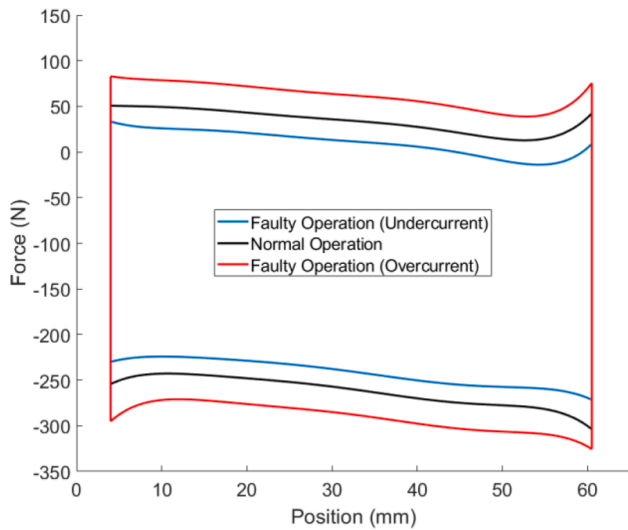


Fig. 7. MR damping force with respect to position when piston velocity is set to 41.5 mm/s.

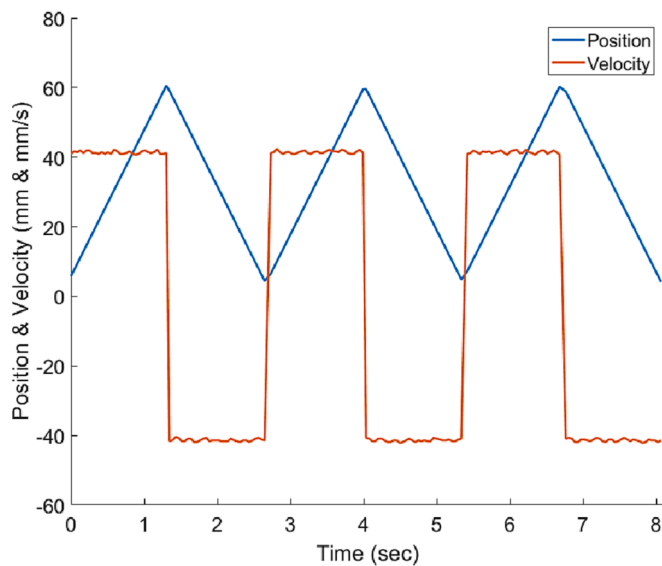


Fig. 8. Sample of experimental data used to model the MR damper under normal operating conditions.

modelling uncertainty in the form of an undercurrent fault (20 mA) was introduced to the MR damper at 5.3 s before completing a final extension and retraction. The undercurrent fault is implemented in an identical fashion as in the case of an overcurrent fault: by adjusting the coefficients of the polynomial according to the values outlined in Table 1.

The time varying boundary layer was recorded in order to determine the threshold for switching between the EKF and ESIF as well as UKF and ESIF. The boundary layer width over the course of the experiment can be visualized in Fig. 9. A threshold of $\delta_{lim} = 200$ was manually selected for the boundary layer width of the third state based on experimental observations throughout the course of this study. Under normal operating conditions, the boundary layer width is normally below this selected threshold. The boundary layer width exceeds this threshold far more frequently in the faulty cases. The fixed constant boundary layer used to compute the gain in the ESIF algorithm was also manually determined and tuned based on our experiments, and is given as follows:

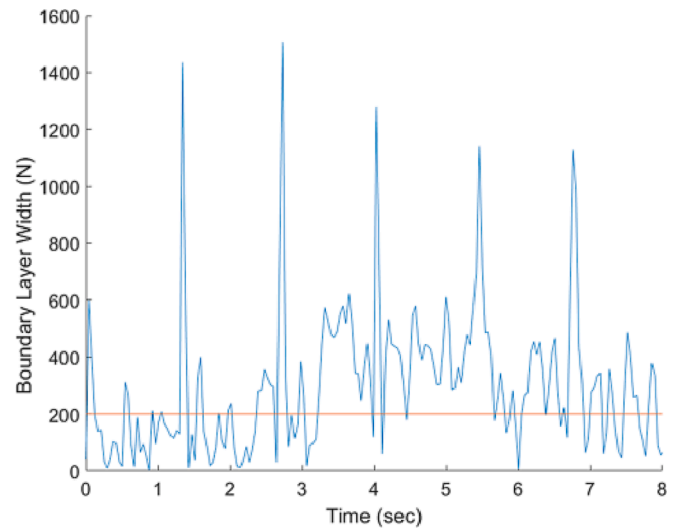


Fig. 9. Time varying boundary layer and boundary layer threshold for determining switching between Kalman filter variants and ESIF.

$$\delta = \begin{bmatrix} 5.5134 \cdot 10^{-4} & 0 & 0 \\ 0 & 7.797 \cdot 10^{-4} & 0 \\ 0 & 0 & 60 \end{bmatrix} \quad (5.1)$$

Preliminary experimental simulations demonstrate that the EKF and UKF both estimate the true force exerted by the MR damper accurately for the normal operating case. This is by virtue of both filters heavy reliance on the system model. The EKF-ESIF and UKF-ESIF have moderate performance in the normal case and begin to exhibit deviation from the true state when the measurement noise is high. The RMSE (root mean squared error) was calculated as follows:

$$RMSE = \sqrt{\frac{\sum_{i=1}^n (x_i - \hat{x}_i)^2}{n}} \quad (5.2)$$

where i is the time step, n is the number of steps, x_i is the true damping force, and \hat{x}_i is the estimated damping force. Table 2.

shows the RMSE for the normal case. Twenty separate trials were conducted and the RMSEs for each test were averaged to form Tables 2 and 3.

The filter performance of mixed operation in which the MR damper experiences normal, overcurrent, and undercurrent modes is shown in Fig. 10. In this case, combining the ESIF with the EKF and UKF results in significantly improved state estimation as shown by Table 3. While the UKF performed better than the EKF, the EKF-ESIF and UKF-ESIF performed comparatively. The combined ESIF strategy shows more robustness in the presence of modeling uncertainty caused by faults in the system. The standard EKF and UKF are unable to compensate for the modeling uncertainty which results in estimates that are very close to the system model for the normal case. In Fig. 11, the estimation error for each filtering strategy is depicted. When sensor noise is high in the normal case, the combined estimation strategies occasionally use the SIF gain which is suboptimal for well-defined systems. However, the SIF consistently performs better than the UKF when modeling uncertainties

Table 2
RMSE for normal operation.

Estimation Strategy	RMSE (Newtons)
EKF	2.81
UKF	2.74
EKF-ESIF	6.89
UKF-ESIF	6.79

Table 3
RMSE for mixed operation.

Estimation Strategy	RMSE (Newtons)
EKF	20.39
UKF	18.36
EKF-ESIF	13.71
UKF-ESIF	13.22

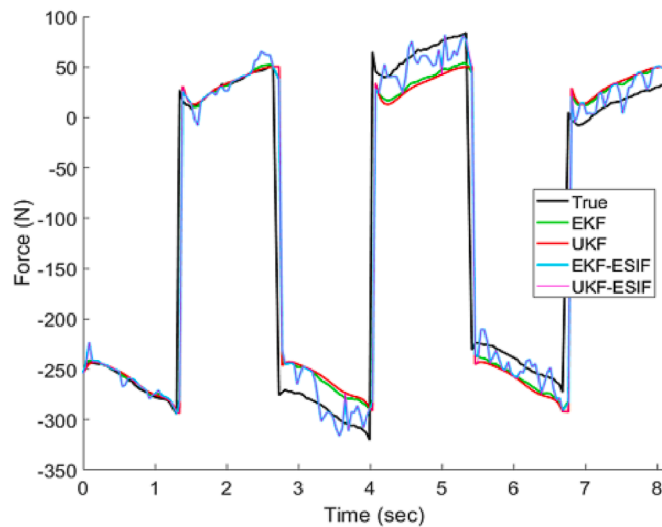


Fig. 10. Force estimation of the MR damper undergoing mixed operation with normal, overcurrent, and undercurrent modes.

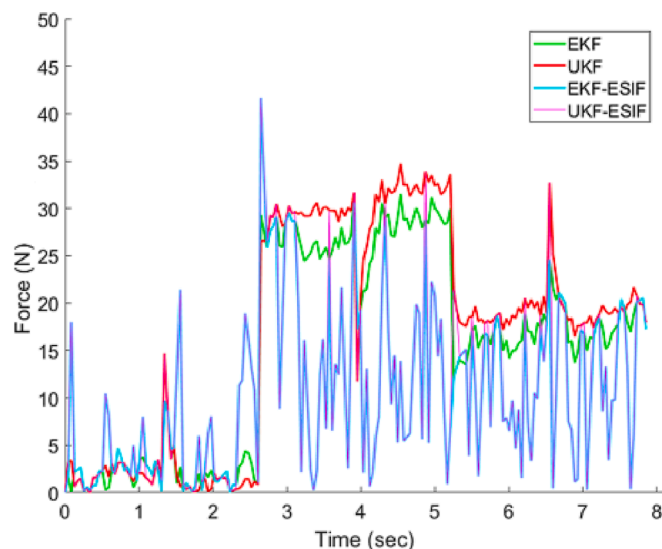


Fig. 11. Force estimation error for an MR damper undergoing mixed operation with normal, overcurrent, and undercurrent modes.

are introduced.

In addition, the high-frequency switching behavior of the SIF gain resulting in chattering can also be witnessed in the plot of the time varying boundary layer in Fig. 9, as well as in the estimator errors in Fig. 11. This behavior has been attributed to the fact that the state estimates may grow beyond the size of the boundary layer, and then suddenly return within the boundary layer upon the triggering of the adaptive gain. As such, a simple thresholding-based approach as can be seen in Fig. 9 is associated with a limitation of the adaptive SIF-KF approach. These findings are consistent with that of the SVSF and its

adaptive formulation: the SVSF-KF [14]. In [14], the authors propose modifying the adaptive gain formulation by exploring several alternative formulations based on the normalized innovation squares (NIS) metric, the multiple model adaptive estimator (MMAE), and the interacting multiple model (IMM) frameworks. We therefore postulate that the dramatic fluctuation of the estimator error witnessed in this study can be addressed similarly as in [14], and consider this to be a significant area of future research which we plan to undertake in future studies.

6. Conclusions

In this paper, a combined Kalman and sliding innovation filtering strategy is presented. The criterion for switching between the filters was based on the time-varying sliding boundary layer that is utilized by the SIF. A trade-off exists between robustness to uncertainties and estimation accuracy. In this case, the proposed EKF-ESIF and UKF-ESIF strategies sacrifice some estimation accuracy for robustness to uncertainties such as system faults. The experiment described in this paper is a challenging estimation scenario and may be used for future research as it serves as a highly repeatable benchmark. For an MR damper undergoing mixed operation (which adds modeling uncertainty), the proposed EKF-ESIF and UKF-ESIF strategies demonstrated improved estimation performance over their standard counterparts by about 28 % for the EKF and 33 % for the UKF on average (for force estimation). The ESIF can be expanded further to improve estimation performance as it currently uses a first order Taylor series approximation of the nonlinear system model and measurement process. Instead, an iterative extended Kalman filter (IEKF) which recursively updates the point at which the system is linearized around could also be implemented for the ESIF to better approximate nonlinear dynamics.

We have also identified several promising avenues for future research based on the findings presented in this study. First, the chattering issue encountered due to the high-frequency gain switching will be addressed by investigating alternate strategies for triggering the adaptive gain. Examples of such alternate strategies include the NIS metric, a statistical-based thresholding approach, or probabilistic frameworks like the MMAE and IMM. These strategies have been selected based on their success in being implemented in a similar manner on the adaptive SVSF-KF approach. Secondly, future studies will also investigate a wider range of fault types, operating conditions and variable factors relating to the MR damper test bed. Such examples include other types of faults not related to the power supply, consideration of non-constant variables like velocity, temperature, pressure, and more. Finally, these future studies will include a comprehensive exposition of the SVSF and SIF's adaptive formulations to confirm the SIF's improved estimation performance.

CRediT authorship contribution statement

Andrew S. Lee: Conceptualization, Methodology, Software, Investigation, Writing – original draft. **Waleed Hilal:** Methodology, Investigation, Writing – review & editing. **S. Andrew Gadsden:** Conceptualization, Investigation, Writing – review & editing, Supervision, Project administration, Funding acquisition. **M. Al-Shabi:** Investigation, Writing – review & editing, Supervision.

Declaration of Competing Interest

The authors declare that they have no known competing financial interests or personal relationships that could have appeared to influence the work reported in this paper.

Data availability

Data will be made available on request.

References

- [1] H.H. Afshari, S.A. Gadsden, S. Habibi, Gaussian filters for parameter and state estimation: a general review of theory and recent trends, *Signal Process.* 135 (2017) 218–238, <https://doi.org/10.1016/j.sigpro.2017.01.001>.
- [2] B. Ristic, S. Arulampalam, *Beyond the Kalman Filter: Particle Filters for Tracking Applications*, vol. 685, Artech House, Boston, MA, 2004.
- [3] S. Haykin (Ed.), *Kalman Filtering and Neural Networks*, John Wiley & Sons, Inc., New York, USA, 2001.
- [4] N. Alsadi, et al., Neural network training loss optimization utilizing the sliding innovation filter, in: T. Pham, L. Solomon, M.E. Hohil (Eds.), *Artificial Intelligence and Machine Learning for Multi-Domain Operations Applications IV*, SPIE, 2022, p. 76, <https://doi.org/10.1117/12.2619029>.
- [5] S.A. Gadsden, Y. Song, S.R. Habibi, Novel model-based estimators for the purposes of fault detection and diagnosis, *IEEE/ASME Trans. Mechatron.* 18 (4) (2013), <https://doi.org/10.1109/TMECH.2013.2253616>.
- [6] Y. Cao, X. Bu, M. Xu, H. Yang, Infrared focal plane array attitude measurement method based on adaptive fault-tolerant extended Kalman filter, *Measurement (Lond.)* 176 (2021), 109172, <https://doi.org/10.1016/j.measurement.2021.109172>.
- [7] X. Yin, H. Chai, M. Xiang, Z. Du, X. Tian, A GEO-pivoted adaptive extended Kalman filtering method in low-latitude dense building environment, *Measurement (Lond.)* 173 (2021), 108657, <https://doi.org/10.1016/j.measurement.2020.108657>.
- [8] S.A. Gadsden, S. Habibi, T. Kirubarajan, Kalman and smooth variable structure filters for robust estimation, *IEEE Trans. Aerosp. Electron. Syst.* 50 (2) (2014), <https://doi.org/10.1109/TAES.2014.110768>.
- [9] S.K. Spurgeon, Sliding mode observers: a survey, *Int. J. Syst. Sci.* 39 (8) (2008), <https://doi.org/10.1080/00207720701847638>.
- [10] D. Simon, Optimal state estimation: Kalman, H_∞, and nonlinear approaches. 2006. doi: 10.1002/0470045345.
- [11] J.-J. Slotine, *Applied Nonlinear Control*, Prentice-Hall, Eaglewood Cliffs, NJ, 2001.
- [12] S.A. Gadsden, A.S. Lee, Advances of the smooth variable structure filter: square-root and two-pass formulations, *J. Appl. Remote Sens.* 11 (1) (2017) pp, <https://doi.org/10.1117/1.jrs.11.015018>.
- [13] M. Alshabi, A. Elnady, Recursive smooth variable structure filter for estimation processes in direct power control scheme under balanced and unbalanced power grid, *IEEE Syst. J.* 14 (1) (2020), <https://doi.org/10.1109/JSYST.2019.2919792>.
- [14] J. Goodman, W. Hilal, S.A. Gadsden, C.D. Eggleton, Adaptive SVSP-KF estimation strategies based on the normalized innovation square metric and IMM strategy, *Results Eng.* 16 (2022), 100785, <https://doi.org/10.1016/j.rineng.2022.100785>.
- [15] S. Andrew Gadsden, M. Al-Shabi, The Sliding Innovation Filter, *IEEE Access*, vol. 8, 2020, doi: 10.1109/ACCESS.2020.2995345.
- [16] A.S. Lee, S.A. Gadsden, M. Al-Shabi, An adaptive formulation of the sliding innovation filter, *IEEE Signal Process Lett.* 28 (2021) 1295–1299, <https://doi.org/10.1109/LSP.2021.3089918>.
- [17] W. Hilal, S. A. Gadsden, S. A. Wilkerson, M. A. Al-Shabi, A square-root formulation of the sliding innovation filter for target tracking, 2022. doi: 10.1117/12.2618965.
- [18] W. Hilal, S. A. Gadsden, S. A. Wilkerson, M. A. Al-Shabi, Combined particle and smooth innovation filtering for nonlinear estimation, 2022. doi: 10.1117/12.2618973.
- [19] Y. Huang, Y. Zhang, Z. Wu, N. Li, J. Chambers, A novel adaptive Kalman filter with inaccurate process and measurement noise covariance matrices, *IEEE Trans Automat Contr* 63 (2) (2018), <https://doi.org/10.1109/TAC.2017.2730480>.
- [20] Y. Huang, F. Zhu, G. Jia, Y. Zhang, A slide window variational adaptive Kalman filter, *IEEE Trans. Circ. Syst. Exp. Briefs* 67 (12) (2020), <https://doi.org/10.1109/TCSII.2020.2995714>.
- [21] Y. Huang, Y. Zhang, J.A. Chambers, A novel Kullback-Leibler divergence minimization-based adaptive student's t-filter, *IEEE Trans. Signal Process.* 67 (20) (2019) pp, <https://doi.org/10.1109/TSP.2019.2939079>.
- [22] Y. Huang, Y. Zhang, Y. Zhao, J.A. Chambers, A novel robust gaussian-student's t mixture distribution based Kalman filter, *IEEE Trans. Signal Process.* 67 (13) (2019), <https://doi.org/10.1109/TSP.2019.2916755>.
- [23] F. Zhu, Y. Huang, C. Xue, L. Mihaylova, J. Chambers, A sliding window variational outlier-robust Kalman filter based on student's t-noise modeling, *IEEE Trans. Aerosp. Electron. Syst.* 58 (5) (2022), <https://doi.org/10.1109/TAES.2022.3164012>.
- [24] Y. Huang, Y. Zhang, Y. Zhao, P. Shi, J.A. Chambers, A novel outlier-robust kalman filtering framework based on statistical similarity measure, *IEEE Trans. Autom. Contr.* 66 (6) (2021), <https://doi.org/10.1109/TAC.2020.3011443>.
- [25] Z. Wang, D. Zhou, S. Gong, Uncalibrated visual positioning using adaptive Kalman Filter with dual rate structure for wafer chip in LED packaging, *Measurement (Lond.)* 191 (2022), 110829, <https://doi.org/10.1016/j.measurement.2022.110829>.
- [26] C. Pan, J. Gao, Z. Li, N. Qian, F. Li, Multiple fading factors-based strong tracking variational Bayesian adaptive Kalman filter, *Measurement (Lond.)* 176 (2021), 109139, <https://doi.org/10.1016/j.measurement.2021.109139>.
- [27] W. Shi, J. Xu, H. He, D. Li, H. Tang, E. Lin, Fault-tolerant SINS/HSB/DVL underwater integrated navigation system based on variational Bayesian robust adaptive Kalman filter and adaptive information sharing factor, *Measurement (Lond.)* 196 (2022), 111225, <https://doi.org/10.1016/j.measurement.2022.111225>.
- [28] J. Shao, W.u. Chen, Y.a. Zhang, F. Yu, J. Wang, Adaptive maximum correntropy based robust CKF with variational Bayesian for covariance estimation, *Measurement (Lond.)* 202 (2022), 111834, <https://doi.org/10.1016/j.measurement.2022.111834>.
- [29] X. Dong, G. Chen, X. Tian, X. Yan, Real-time estimation of roll angles by magnetometer based on two-step adaptive Kalman filter, *Measurement (Lond.)* 198 (2022), 111349, <https://doi.org/10.1016/j.measurement.2022.111349>.
- [30] LORD RD-8041-1 MR Damper. <<https://www.shoplordmr.com/mr-products/rd-8041-1-mr-damper-long-stroke>> (Accessed May 24, 2023).
- [31] J.S. Oh, K.S. Kim, Y.S. Lee, S.B. Choi, Dynamic simulation of a full vehicle system featuring magnetorheological dampers with bypass holes, *J. Intell. Mater. Syst. Struct.* 31 (2) (2020) pp, <https://doi.org/10.1177/1045389X19876880>.
- [32] "UltraMotion A1-actuator. <<https://www.ultramotion.com/linear-actuators/attachment/a1-actuator/>> (Accessed May 24, 2023).
- [33] "Loadstar RAS1 S-Beam Load Cell, <<https://www.loadstarsensors.com/ras1-s-beam-load-cell.html>> (Accessed May 24, 2023).
- [34] M.K. Thakur, C. Sarkar, Influence of graphite flakes on the strength of magnetorheological fluids at high temperature and its rheology, *IEEE Trans. Magn.* 56 (5) (2020) pp, <https://doi.org/10.1109/TMAG.2020.2978159>.
- [35] X.Q. Ma, S. Rakheja, C.Y. Su, Development and relative assessments of models for characterizing the current dependent hysteresis properties of magnetorheological fluid dampers, *J. Intell. Mater. Syst. Struct.* 18 (5) (2007) pp, <https://doi.org/10.1177/1045389X06067118>.
- [36] S.B. Choi, S.K. Lee, Y.P. Park, A hysteresis model for the field-dependent damping force of a magnetorheological damper, *J. Sound Vib.* 245 (2) (2001) pp, <https://doi.org/10.1006/jsvi.2000.3539>.
- [37] J.S. Kumar, P.S. Paul, G. Raghunathan, D.G. Alex, A review of challenges and solutions in the preparation and use of magnetorheological fluids, *Int. J. Mech. Mater. Eng.* 14 (1) (2019) pp, <https://doi.org/10.1186/s40712-019-0109-2>.